SUPERSONIC FLIGHT DYNAMICS TEST 2: TRAJECTORY, ATMOSPHERE, AND AERODYNAMICS RECONSTRUCTION

Christopher D. Karlgaard[*], **Clara O'Farrell**[†],
Jason M. Ginn[‡], **John W. Van Norman**[§]

The Supersonic Flight Dynamics Test is a full-scale flight test of aerodynamic decelerator technologies developed by the Low Density Supersonic Decelerator technology demonstration project. The purpose of the project is to develop and mature aerodynamic decelerator technologies for landing large-mass payloads on the surface of Mars. The technologies include a Supersonic Inflatable Aerodynamic Decelerator and supersonic parachutes. The first Supersonic Flight Dynamics Test occurred on June 28th, 2014 at the Pacific Missile Range Facility. The purpose of this test was to validate the test architecture for future tests. The flight was a success and, in addition, was able to acquire data on the aerodynamic performance of the supersonic inflatable decelerator. The Supersonic Disksail parachute developed a tear during deployment. The second flight test occurred on June 8th, 2015, and incorporated a Supersonic Ringsail parachute which was redesigned based on data from the first flight. Again, the inflatable decelerator functioned as predicted but the parachute was damaged during deployment. This paper describes the instrumentation, analysis techniques, and acquired flight test data utilized to reconstruct the vehicle trajectory, main motor thrust, atmosphere, and aerodynamics.

INTRODUCTION

The Low Density Supersonic Decelerator (LDSD) project is a NASA technology development program designed to mature aerodynamic decelerator technologies that can be used for landing high mass payloads (beyond the present capability of rigid Viking-derived 70-degree sphere cone entry vehicles) on the surface of Mars.[1] Through a series of extensive ground and flight tests, the following decelerator technologies will be developed: a Supersonic Inflatable Aerodynamic Decelerator for Robotic missions (SIAD-R), a Supersonic Inflatable Aerodynamic Decelerator for Human Exploration missions (SIAD-E), and a supersonic parachute. The flight test campaign, referred to as the Supersonic Flight Dynamics Test (SFDT), exercises the decelerator technologies with several full scale, high-altitude missions at the Pacific Missile Range Facility (PMRF) in Kauai, Hawaii. The first of these tests, SFDT-1, was conducted on June 28, 2014.[2,3] The purpose of the test was to validate the test architecture for future tests. The flight was a success and, in addition, was able to acquire data on the aerodynamic performance of the supersonic inflatable decelerator. The Supersonic Disk Sail parachute developed a tear during deployment, and so performance of this system could not be fully evaluated. Data acquired from the flight test were used to redesign the parachute for future tests, and other lessons learned from the test were used to update certain pre-flight simulation models relating to aerodynamics and flight dynamics.

The SFDT Test Vehicle (TV) configuration is shown in Figure 1. The TV is a 4.7 m diameter aeroshell with a spherical forebody similar in shape to the Apollo command module, with a shoulder radius equivalent to the Mars Science Laboratory entry capsule. The SFDT TV forebody is designed to match the shape of a Mars Design Reference Vehicle (DRV).[4] The SFDT TV outer mold line matches that of the DRV forward of the backshell-heatshield separation plane. The SFDT capsule backshell is removed to accommodate a STAR-48 solid rocket motor and a camera mast. The SIAD-R, shown in its deployed configuration in Figure 1(b), is a 6 m diameter attached torus.

The nominal SFDT-2 flight sequence is illustrated in Figure 2. The sequence begins with the launch of the balloon-carried test vehicle (TV) from the ground. The balloon carries the TV to an altitude of approximately 120,000 ft. The TV is released from the balloon, spin-up motors fire, and a STAR-48 solid rocket motor ignites to carry the vehicle to the desired test condition of 180,000 ft and Mach 4. After the motor burn

---

[*]Supervising Engineer, Analytical Mechanics Associates, Inc., Member AAS, Senior Member AIAA.
[†]Guidance and Control Engineer, Jet Propulsion Laboratory, California Institute of Technology.
[‡]Mechanical Engineer, Jet Propulsion Laboratory, California Institute of Technology.
[§]Senior Project Engineer, Analytical Mechanics Associates, Inc.
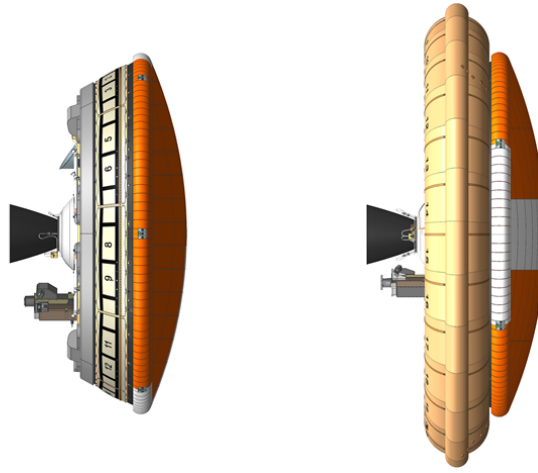
(a) SFDT Powered Flight and Coast Phase Configuration

(b) SFDT SIAD-R Test Phase Configuration

Figure 1: SFDT Test Vehicle Configuration

is complete, the vehicle is de-spun. Upon reaching a predetermined planet-relative velocity, the onboard computer commands the deployment of the SIAD, which begins the test period of the mission. The vehicle decelerates to a condition of Mach 2.5 where the Parachute Deployment Device (PDD) is deployed, extracting the main parachute. The TV remains under the Supersonic Ringsail (SSRS) parachute for the remainder of the flight until landing in the Pacific Ocean.
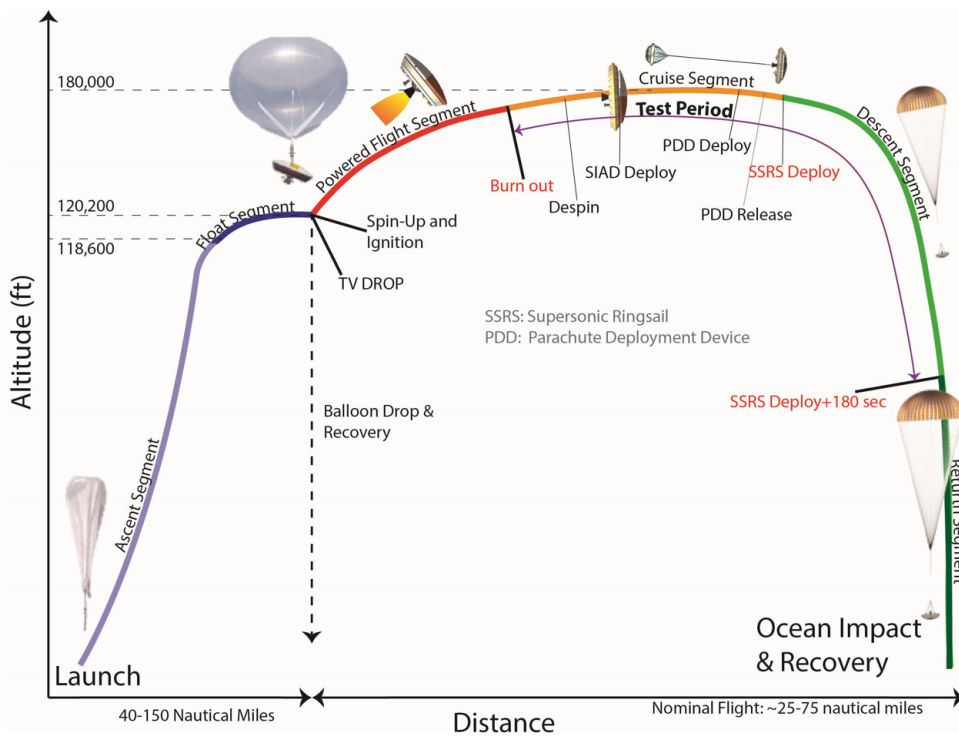

Figure 2: Supersonic Flight Dynamics Test Two Overview

The second flight test occurred on June 8th, 2015 at PMRF. This flight test was similar to the previous test but it incorporated updates to simulations models used for targeting and a redesigned SSRS parachute based on lessons learned from SFDT-1. The flight was nominal until shortly after spin down, where an anomalous disturbance force was encountered that initiated capsule oscillations of up to 30 deg angle of attack. These oscillations reduced the overall drag and thus the vehicle decelerated slower than predicted, increasing the

time between spin down and SIAD deployment. The SIAD deployed successfully, and was also able to reduce the amplitude of the capsule oscillations through its increased static stability. A second force anomaly was encountered shortly after PDD deployment, which introduced a roll rate of 20 deg/s. The parachute was deployed, but again suffered a structural failure and so this technology could not be evaluated. The TV, Flight Imagery Recorder (FIR), PDD, SSRS, balloon carcass and recovery parachute were all recovered after the flight.

This paper describes the data sources and methodology used to reconstruct the SFDT-2 trajectory, atmosphere and aerodynamics. The remainder of the paper is organized as follows. A summary of the sensor measurements available for use in the reconstruction is given and the quality of the measurements from the test flight is described. An overview of the reconstruction methodology and tools is presented. Results of the reconstruction are shown and explored. Additional information about the SFDT-2 flight test can be found in References 5–8, which include pre-flight flight dynamics modeling and simulation,[5] flight test overview,[6] post-flight flight dynamics assessment,[7] and post-flight aerodynamics assessment.[8]

INSTRUMENTATION AND MEASUREMENTS

A variety of measurement sources were available for use in the trajectory and atmosphere reconstruction process. These measurements included onboard instrumentation such as an Inertial Measurement Unit (IMU), Global Positioning System (GPS) receiver, and STAR-48 chamber pressure transducer; ground-based measurements from tracking radars; and atmospheric soundings from balloons and high-altitude rockets. The following sections provide a more detailed overview of the measurement sources and their performance on the day of flight.

Inertial Measurement Unit

Three-axis linear accelerations and angular rates were measured by a Gimbaled LN-200 with Miniature Airborne Computer (GLN-MAC) inertial navigation system. The LN-200 inertial measurement unit contains three-axis solid-state silicon Micro Electro-Mechanical System (MEMS) accelerometers and three-axis solid-state fiber-optic gyroscopes. The GLN-MAC incorporates a roll isolation gimbal to produce a stable platform for spinning vehicle applications. An electric motor is used to counter-rotate the internal mount plate such that the LN-200 senses a low rotational rate about the roll axis. The gimbaling has the effect of reducing error buildup due to scale factor uncertainties in the roll gyro. The angle of the mount plate is measured with a resolver. The GLN-MAC is mounted in the vehicle approximately 0.5 m off the centerline. The GLN-MAC has the capability to "cage" or lock the LN-200 in a preferred orientation, creating a true strapdown IMU. This mode was not used for the SFDT-2 flight; the LN-200 was free to gimbal throughout the entire flight test.

The GLN-MAC produces two sets of telemetry, one from the gimbaled LN-200 at a rate of 400 Hz and one from the integrated GLN-MAC system at a rate of 100 Hz. The resolver angle is also telemetered at a rate of 400 Hz. The GLN-MAC level outputs utilize the resolver angle and resolver rate to generate an equivalent strapdown representation of the gimbaled LN-200 accelerations and rates. Typical performance characteristics of the GLN-MAC sensor can be found in Reference 9. The particular unit used onboard the SFDT-2 flight was thoroughly tested and evaluated, and the reconstruction assumptions were tuned to match the observed performance characteristics of the device (noise and misalignments). The raw LN-200 data was corrected post-flight for known thermal biases and misalignments prior to its use in the trajectory reconstruction. There were no dropped frames or missing data from the GLN-MAC telemetry.

Global Positioning System

Measurements of position and velocity were obtained from a Javad G2T GPS receiver at a rate of 10 Hz. The GPS antennas were located in a diametrically opposed configuration on the shoulder of the vehicle. A pre-flight analysis of the trajectory determined that the GPS receiver would lose lock on the satellites during powered flight due to the high spin rate experienced by the vehicle, which occurred as expected during the SFDT-2 test. The GPS receiver reacquired satellites after spin down and provided valid measurements through the remainder of the trajectory, with the exception of a small dropout at parachute deployment.

The Javad unit also produced estimates of the uncertainties in the position and velocity solution based on the number of satellites in view, shown in Figure 3(a), and the covariance of the onboard solution. The receiver estimates of position and velocity RMS errors are shown in Figure 3(b).
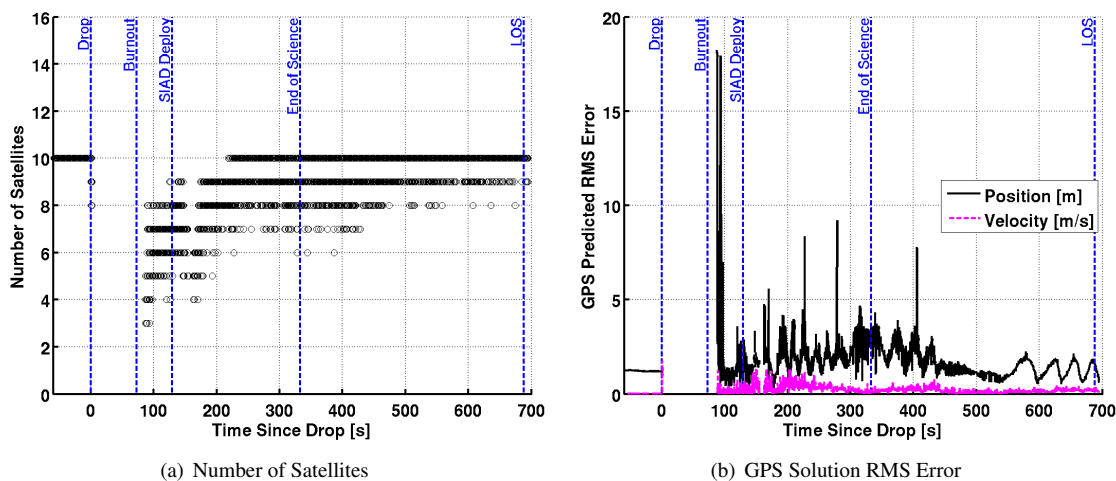
(a) Number of Satellites	(b) GPS Solution RMS Error

Figure 3: GPS Satellites and RMS Errors

Tracking Radar

Range, azimuth, and elevation measurements of the test vehicle were acquired by three ground-based C-Band tracking radars operated by PMRF. Two tracks were provided by beacon tracking Radar Open System Architecture (ROSA) radar stations Queen 2 (Q2) and Queen 8 (Q8) at a rate of 40 Hz. The C-Band radar beacons were mounted in a diametrically opposed configuration on the shoulder of the vehicle. The third track was provided by a wide-band/narrow-band skin tracking Digital-Receiver Coherent Signal Processor (DR-COSIP) radar, Queen 4 (Q4), at a rate of 10 Hz. Additional details of the radars is given in Table 1, and the locations of these radars relative to the as-flown trajectory are shown in Figure 4.

Table 1: Radar Stations

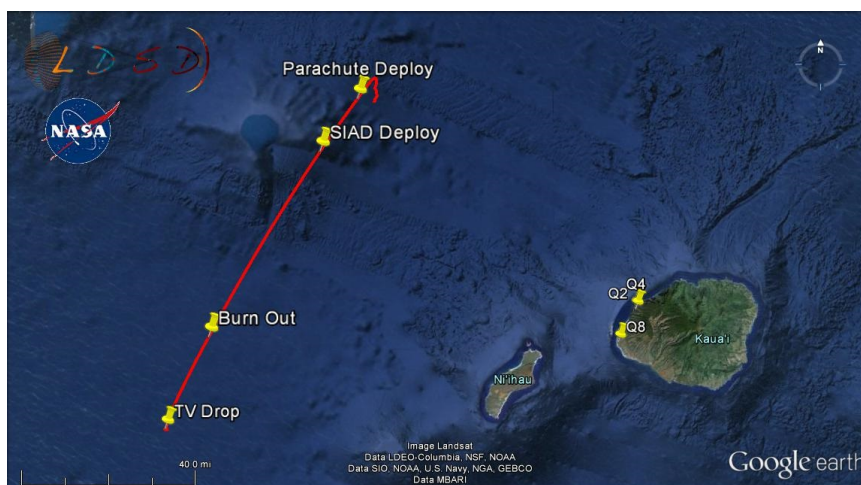| Radar	Architecture	Type	Site	Time Spans (seconds since drop)
Queen 2	ROSA	AN/MPS-25	Makaha Ridge	-60–37, 42–134, 139–265, 270–391, 395–560
Queen 4	DR-COSIP	AN/FPQ-19	Makaha Ridge	-60–0, 30–688.1
Queen 8	ROSA	AN/MPS-25	Barking Sands	-60–15, 30–190, 196–300, 330–570

Figure 4: SFDT-2 Ground Track and Radar Locations

4

In general, the measured radar tracks were of good quality and were in overall agreement. Based on recommendations from PMRF, the wide-band data from Q4 was chosen over the the narrow-band track for trajectory reconstruction because of lower noise and systematic error content.

STAR-48 Chamber Pressure Transducer

A Kulite ETM-HT-375 pressure transducer was installed in the STAR-48 to measure the motor chamber pressure in order to reconstruct the thrust. The transducer was installed in a toroidal ignitor inside the motor, and acquired pressure measurements at a rate of 1041.67 Hz. The transducer was calibrated once by Kulite and again by the STAR-48 manufacturer, ATK, prior to installation in the motor. Uncertainty analysis of the calibration data indicated a 3σ total uncertainty of 99.7 kPa. Note that this is a new measurement source for SFDT-2; a chamber pressure measurement was not available for SFDT-1, and thrust was reconstructed from the measured accelerations and nominal aerodynamics.

Meteorological Data

Atmospheric reconstruction for the SFDT-2 flight included data from meteorological sounding rockets, weather balloons, and from a pressure sensor onboard the vehicle. The rocket sounding was performed by a 1 m diameter mylar PWN-12A Rocket Balloon Instrument (ROBIN) sphere that was launched by a Super Loki rocket. The ROBIN sphere was deployed at apogee, and tracked by radar during descent. The sphere fell until it reached an altitude of 30-35 km where it collapsed due to the ambient pressure. With known drag characteristics, the atmospheric density and winds were estimated from the radar track.

Each weather balloon carried a Vaisala RS-92 radiosonde. The RS-92 contained a capacitive wire temperature sensor, a Barocap silicon capacitive pressure sensor, a thin-film capacitive humidity sensor, and a GPS receiver. Winds were derived using the GPS measurements.

A pair of variable inductance pressure transducers mounted on the aft of the vehicle were also used to aid atmospheric reconstruction. The pressure reading just prior to test vehicle drop was used to anchor the upper atmosphere reconstruction by providing a measurement at the correct location and time.

In total, two balloon releases and four rocket launches were performed for the SFDT-2 flight. The timeline of launches is shown in Table 2. All four ROBIN spheres deployed successfully; however the third sphere collapsed early at 38.5 km.

Table 2: SFDT-2 Atmospheric Measurement Timeline with Significant SFDT Events in Bold.

Time (HST)	Event
05:59	Weather balloon 1 launched
07:45	SFDT Liftoff
08:45	Sounding rocket 1 launched
08:59	Weather balloon 2 launched
09:15	Sounding rocket 2 launched
11:35	**SFDT dropped from balloon**
11:51	**SFDT splashdown**
12:35	Sounding rocket 3 launched
13:05	Sounding rocket 4 launched

Of the balloon and sounding rocket launches, only data from the second balloon and third rocket were incorporated into the atmospheric reconstruction. These data were chosen because the measurement time was closest to the time of the SFDT flight operations. Below the collapse altitude of the third ROBIN sphere, the data from the fourth sphere were used.

RECONSTRUCTION METHODS

The instrumentation utilized during the SFDT-2 mission provided an extensive set of measurement data from which reconstruction was performed. The following section describes the methodologies used to reconstruct the trajectory, atmosphere and aerodynamics given the measurements taken during flight.

Atmosphere Reconstruction

Upper atmosphere characterization was done using data from the Super Loki rocket with PWN-12A ROBIN sphere payload, anchored to the measurement by the onboard pressure sensors prior to drop. Atmospheric conditions in the lower atmosphere were based on radiosonde data. The density and winds were

determined using the radar tracking data, assuming known drag coefficient, pressure at the lowest altitude (based on onboard pressure transducers), and an initial guess of the atmospheric density profile. For this work, the Mass Spectrometer and Incoherent Scatter (MSIS-E-90) atmosphere profile[10] was used as the initial guess for the density profile.

The ROBIN sphere data provided an incremental density profile relative to the assumed initial density profile. The incremental density was then anchored to the pressure sensor measurement at the lowest ROBIN Sphere altitude (referred to as the tie-on altitude) to produce accurate density values. For this process, temperatures were derived from the ROBIN sphere density profile by assuming the atmosphere was in a state of hydrostatic equilibrium.

Below the tie-on altitude, the atmosphere was based on the measurements collected by the radiosonde. These included altitude and temperature measurements via GPS and capacitive wire sensors, respectively. For the few kilometers between the highest radiosonde measurement and the drop altitude (where the onboard pressure measurement was taken), the ROBIN sphere data were used and smoothing was applied to prevent a discontinuity at the drop altitude. This discontinuity in pressure was likely caused by the difference in time between measurements.

Trajectory Reconstruction

The SFDT-2 trajectory reconstruction was performed using a Matlab-based Iterative Extended Kalman Filter (IEKF) code known as NewSTEP.[11–14] This software is a generalization of the Statistical Trajectory Estimation Program (STEP)[15, 16] that was developed by NASA Langley Research Center and applied to launch and entry vehicle trajectory reconstruction analyses during the 1960s-1980s. The NewSTEP code borrows largely from STEP, but includes various enhancements to the core code that have been developed to accommodate the reconstruction needs of recent flight projects, including SFDT-1.[2]

Several modifications were made to the core code to accommodate unique inputs and outputs for the SFDT flights. The most significant of these modifications was an improved post-processing model used to handle the IMU measurements, which were complicated by the presence of the gimbaled system. Many past applications of gimbaled IMU reconstructions have made use of an equivalent strapdown representation of the linear accelerations and angular rates in the estimation filter by transforming the platform data into a strapdown frame via the measured gimbal angle.[17, 18] This approach has the advantage of producing a strapdown representation of the inertial measurements without any error buildup due to roll gyro scale factor. The drawback to this method is that resolver angular rate and acceleration uncertainty will degrade the measurements substantially due to resolver angle quantization, amplified by errors from numerical differentiation.

For the SFDT flight reconstructions, an alternate approach was devised in which the trajectory of the LN-200 itself was reconstructed from the measurement data using the Kalman filter approach to blend IMU measurements with GPS and Radar. The output of this process is a kinematic reconstructed trajectory of the LN-200 in an IMU-relative frame through inertial space. After reconstructing the LN-200 trajectory, the resolver angle profile is used to transform the state outputs into the vehicle aerodynamic coordinate frame as shown in Figure 5. Additionally, the reconstructed mass properties are incorporated in order to translate the reconstructed state of the vehicle to the center of gravity (CG). The vehicle mass properties used for the reconstruction were computed using pre-flight mass models that were adjusted to match the as-flown timeline.

At this point in the process, the resolver quantization uncertainty corrupts the reconstructed vehicle state, but this uncertainty is an algebraic mapping at each instant in time such that the resolver angle uncertainties do not propagate over time. After transforming the LN-200 state to the vehicle body frame at the CG, the freestream atmosphere is computed as a function of altitude from a table lookup, and the atmospheric relative state (angle of attack, Mach number, dynamic pressure, etc.) and thrust is reconstructed from the STAR-48 chamber pressure measurement. Lastly, vehicle aerodynamics are computed from the CG accelerations, reconstructed thrust (during powered phase) and body rates. A flow diagram of the overall trajectory reconstruction process is shown in Figure 6.
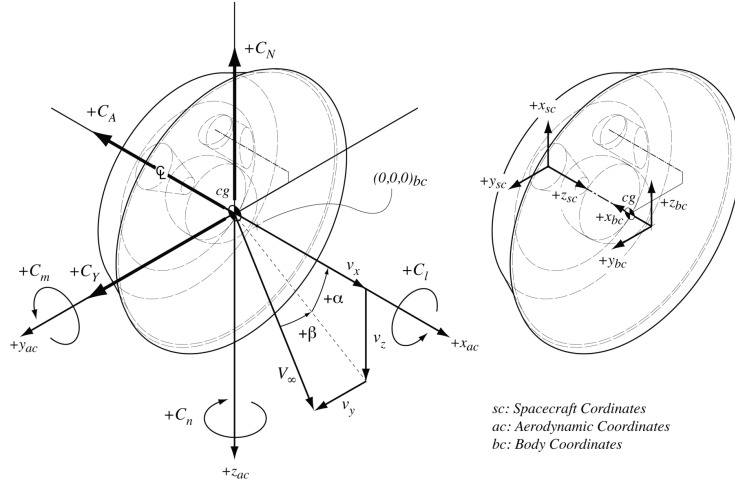
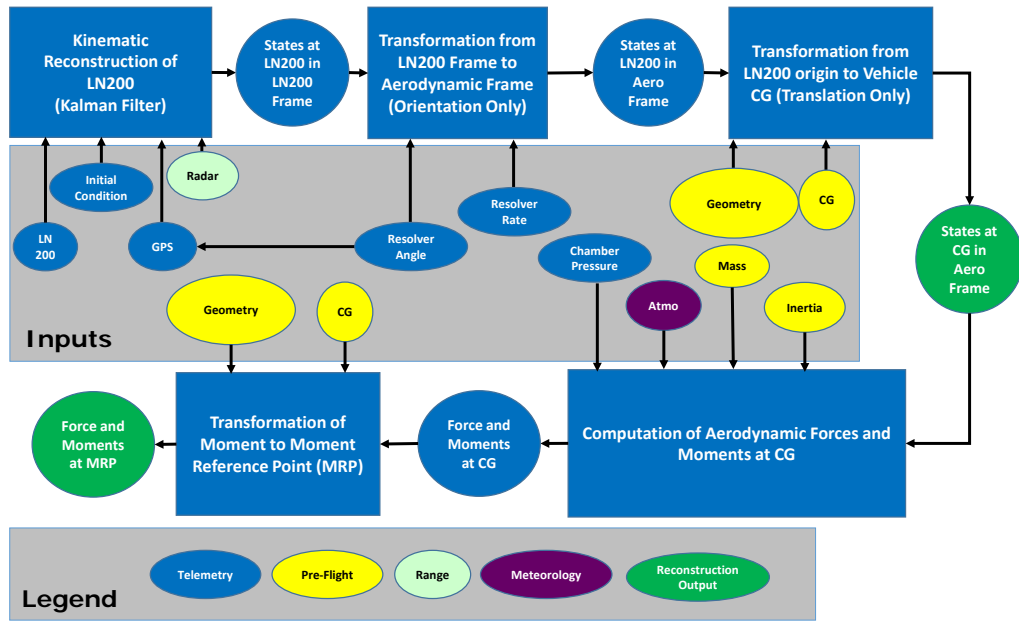**Figure 5**: Test Vehicle Flight Dynamics Coordinate Frames

Figure 6: Reconstruction Flow

STAR-48 Thrust Reconstruction

For SFDT-2, two independent methods were implemented for the STAR-48 main motor thrust reconstruction. The first of these follows the same approach developed for SFDT-1, in which the thrust is solved for from the reconstructed sensed accelerations and the nominal vehicle mass and aerodynamics. The reconstructed vacuum thrust is computed from the relation*

$$T_a = \left\| m \left\{ \begin{array}{c} a_x \\ a_y \\ a_z \end{array} \right\} - \frac{1}{2}\rho V^2 S \left\{ \begin{array}{c} -C_A\left(\alpha, \beta, \mathcal{M}\right) \\ C_Y\left(\alpha, \beta, \mathcal{M}\right) \\ -C_N\left(\alpha, \beta, \mathcal{M}\right) \end{array} \right\} \right\| + P_e A_e \qquad (1)$$

The second method makes use of the STAR-48 chamber pressure measurement to compute the thrust, using the equation[19]

$$T_p = C_F A_t P_c \qquad (2)$$

---

*All of the mathematical symbols used are listed in the Notation section at the end of the paper.

The thrust coefficient and throat area were based on tabulated data provided by ATK, which accounts for real gas effects and throat erosion over time.

Aerodynamic Parameter Estimation

The vehicle aerodynamic force and moment coefficients were calculated from the linear and angular accelerations (after transformation from the LN-200 to the vehicle aerodynamic frame), reconstructed dynamic pressure, vehicle mass, reference area, and reference length using basic aerodynamic relations given by

$$
\left\{ \begin{array}{c} C_A \\ C_Y \\ C_N \end{array} \right\} = \frac{2m}{\rho V^2 S} \left(\frac{1}{m} \left\{ \begin{array}{c} T_p \\ 0 \\ 0 \end{array} \right\} - \left\{ \begin{array}{c} a_x \\ -a_y \\ a_z \end{array} \right\} \right) \tag{3}
$$

$$
\left\{ \begin{array}{c} C_l \\ C_m \\ C_n \end{array} \right\} = \frac{1}{Sqd} \left(\mathcal{I}\dot{\boldsymbol{\omega}} + \boldsymbol{\omega} \times \mathcal{I}\boldsymbol{\omega} \right) \tag{4}
$$

The reconstructed aerodynamics were reconciled with the preflight aerodynamic database by using a parameter estimation technique to solve for a set of dispersions that best fit the reconstructed trajectory. An equation error[20] approach was utilized to estimate parameters of the aerodynamic database that best fit the reconstructed total force and moment coefficients. The aerodatabase has the functional form

$$
\begin{aligned}
C_A &= C_A\left(\alpha, \beta, \mathcal{M}, \boldsymbol{u}\right) & (5) \\
C_Y &= C_Y\left(\alpha, \beta, \mathcal{M}, \boldsymbol{u}\right) & (6) \\
C_N &= C_N\left(\alpha, \beta, \mathcal{M}, \boldsymbol{u}\right) & (7) \\
C_l &= C_l\left(\alpha, \beta, \mathcal{M}, \boldsymbol{u}\right) & (8) \\
C_m &= C_m\left(\alpha, \beta, \mathcal{M}, V, q, \dot{\alpha}, \boldsymbol{u}\right) & (9) \\
C_n &= C_n\left(\alpha, \beta, \mathcal{M}, V, r, \dot{\beta}, \boldsymbol{u}\right) & (10)
\end{aligned}
$$

The vehicle aerodynamic coefficients are functions of the flight condition and the uncertainty factors, $\boldsymbol{u}$. Note that the velocity and rate inputs to the pitch and yaw moments are used in relation to the aerodynamic damping. The uncertainty factors can be used to disperse the aerodynamics for Monte Carlo flight dynamics simulations. Alternately, the uncertainty factors can be viewed as parameters that can be computed in order to best fit the reconstructed aerodynamics. These parameters include various adders and multipliers on the static and dynamic aerodynamics. The reconciled set of uncertainty factors are computed using a nonlinear least squares method to determine the best fit to the reconstructed total force and moment coefficients. The dispersions are constrained such that the pitch and yaw moment multipliers are equal, the side and normal force multipliers are equal, and the pitch and yaw moment dynamic derivatives are equal. The associated adders are unconstrained. These constraints are valid for an axisymmetric vehicle.

FLIGHT DATA ANALYSIS

This section describes the application of the methods described in the previous section to the reconstruction of the trajectory, atmosphere, thrust, and aerodynamics of the SFDT-2 test vehicle.

Reconstructed Atmosphere

Figure 7 shows the reconstructed atmosphere profile based on the PWN-12A ROBIN sphere measurements, the RS-92 radiosonde, and the onboard pressure measurement. For comparison, the atmosphere based on the Earth Global Reference Atmosphere Model (GRAM)[21] is also shown. The altitudes of several important events along the reconstructed SFDT-2 flight path are indicated. For the altitudes corresponding to the SFDT-2 flight path, the reconstructed atmospheric density was up to two and a half standard deviations below the nominal GRAM profile. The temperature profile is fairly consistent with the nominal GRAM atmosphere at the relevant altitudes.

The reconstructed horizontal wind profiles are shown in Figure 8. These were based on ROBIN sphere radar tracking and radiosonde GPS data[†]. The reconstructed wind data is generally consistent with the nominal GRAM profile.

The uncertainties of the atmospheric reconstruction shown here are based solely on instrumentation error specifications and do not include estimates of any potential spatial or temporal perturbations that may occur due to wind gusts or density pockets.

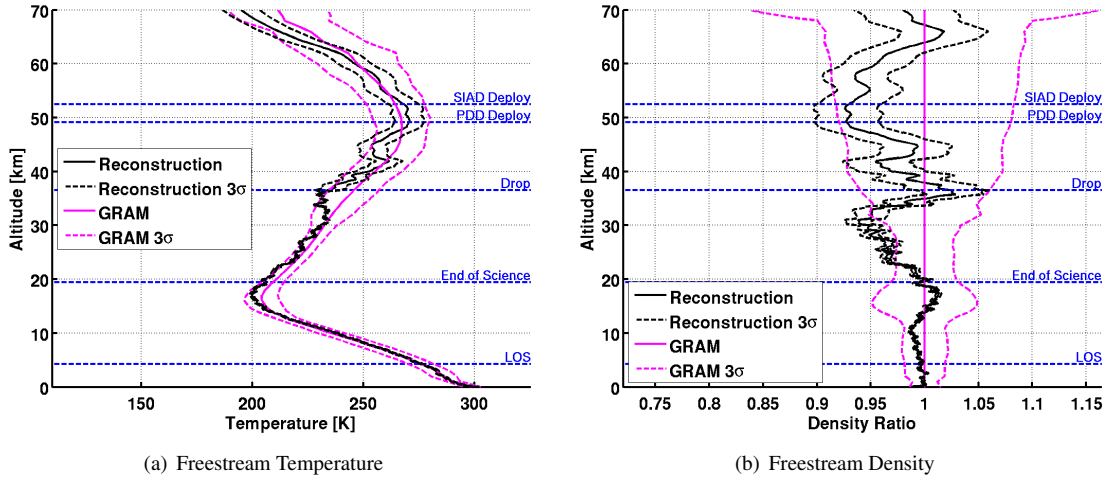[†]The sounding rocket wind profiles were provided to the reconstruction team by the range meteorology group.

(a) Freestream Temperature

(b) Freestream Density

Figure 7: Reconstructed Atmosphere States
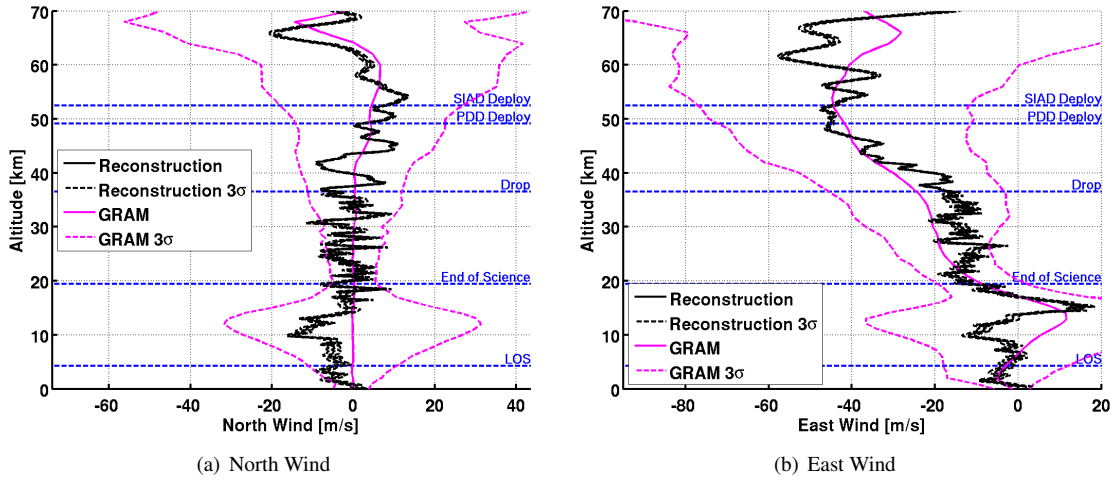

(a) North Wind

(b) East Wind

Figure 8: Reconstructed Winds

Reconstructed Trajectory

The test vehicle trajectory was reconstructed from the LN-200 accelerations and angular rates, GPS, and radar measurements following the process described previously. The reconstruction was initialized 60 seconds before test vehicle drop, based on GPS position and velocity and the GLN-MAC on-board attitude estimate. Reconstruction of state variables was performed until loss of signal at 688.1 seconds and an altitude of approximately 4227 meters. The acceleration and angular rate measurements were filtered using the low pass Fourier filter found in the System Identification Program for Aircraft (SIDPAC)[20] analysis tools. Filtering was performed at 10Hz to remove measurement noise and structural vibration.

The GPS data and uncertainties from the Javad output were used from the initial reconstruction time, 60 seconds before drop, until loss of signal. Some data editing was performed to exclude tracking data from the radar that were not physically consistent with the measured vehicle dynamics, as is typically done with post-test trajectory reconstruction.[13] Radar fit span times are provided in Table 1. Radar measurement biases were included in the state space as solve-for parameters to be estimated in the filter.

The radar and GPS measurement residuals are shown in Figures 9 and 10. The residuals are computed by subtracting the measurement observed during flight from the predicted measurement generated by the filter. An inspection of the measurement residuals provides an assessment of the filter performance relative to the measurement uncertainties. Note that specific periods exist where residual values exceed the 3σ bounds. This behavior is most prominent near particular events in the trajectory such as SIAD deployment, PDD

9

deployment and SSDS deployment, where measurement errors can grow due to the vehicle dynamics. In spite of these deviations, the measurement residuals indicate that the state estimates properly reconciled the radar and GPS measurements.
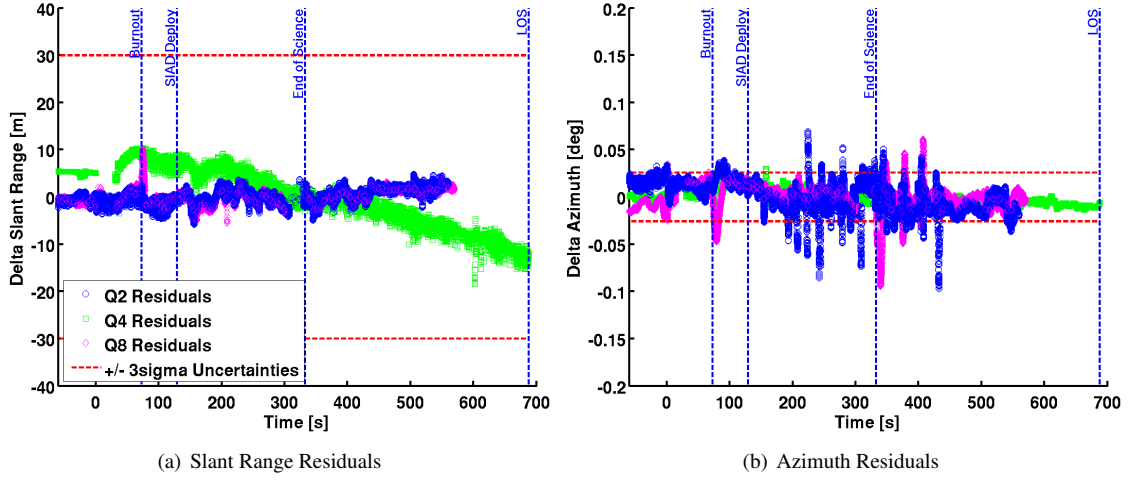

(a) Slant Range Residuals

(b) Azimuth Residuals
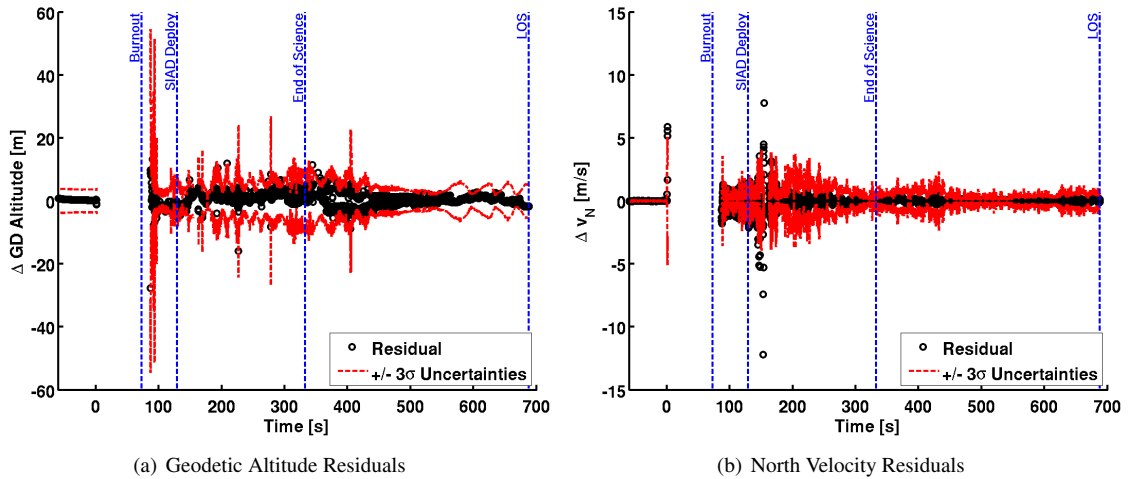
Figure 9: Radar Measurement IEKF Residuals

(a) Geodetic Altitude Residuals

(b) North Velocity Residuals

Figure 10: GPS Measurement IEKF Residuals

After the kinematic reconstruction of the LN-200 was completed by the filter, the measured GLN-MAC resolver angle and reconstructed mass properties profiles were used to transform the reconstructed LN-200 state to the vehicle CG. The reconstructed mass properties were based on pre-flight simulation models that were adjusted to the as-flown timeline. The reconstructed altitude was used to look up atmospheric properties in order to compute atmospheric-relative states, and vehicle aerodynamics. The reconstructed time histories of geodetic altitude, Mach number and dynamic pressure are shown in the left column of Figure 11. Total angle of attack during powered flight and angle of attack and sideslip during SIAD flight are shown in the right column of Figure 11.

The most notable off-nominal behavior of the SFDT-2 trajectory was the large angle of attack and angle of sideslip oscillations that occurred shortly after spin down, which continued throughout the coast phase and into the SIAD phase. These oscillations were produced by an anomalous acceleration, which is shown in Figure 12(a). The anomalous acceleration is characterized by a combination of several seconds of high frequency noise and a thrust-like force that acts on the vehicle over a period of approximately 1 second. The abrupt increase in noise can clearly be seen in the unfiltered accelerations in Figures 12(a) and 12(a)(c) at a time of approximately 73 s after drop. The noise continues through the spin down motor firing. At 74.8 s,
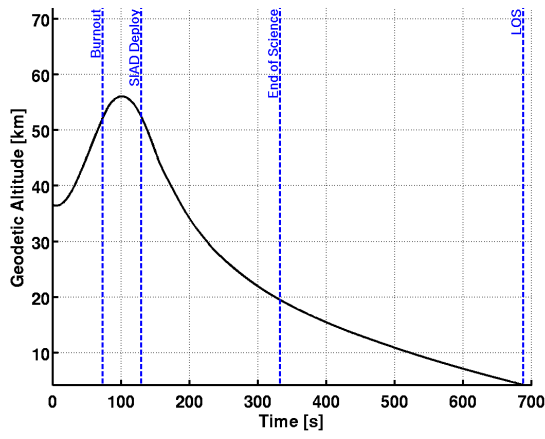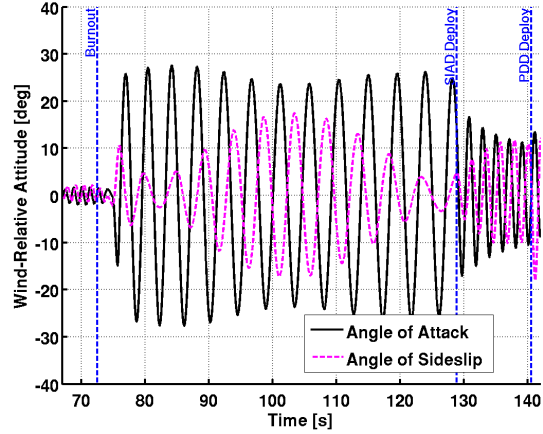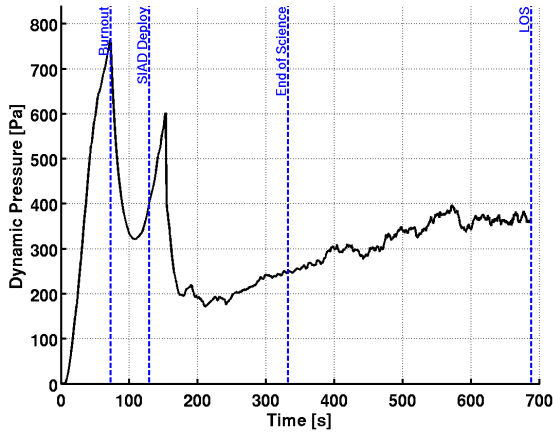
(a) Geodetic Altitude
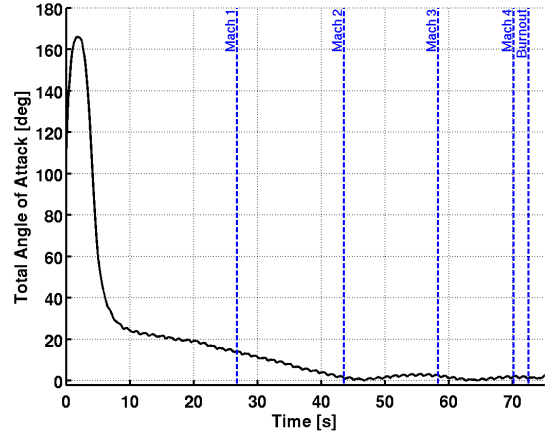
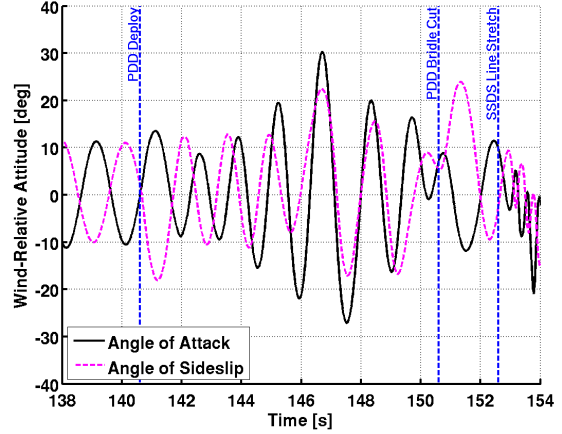(b) Total Angle of Attack - Powered Flight
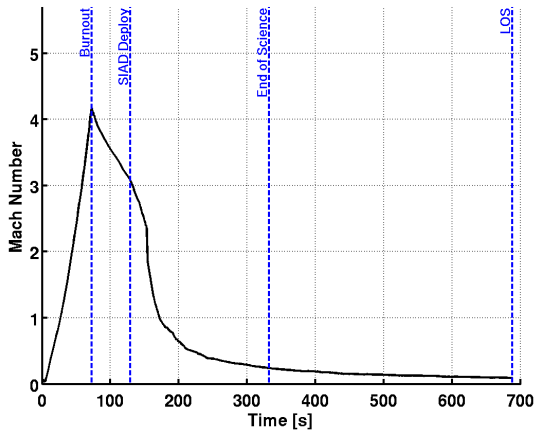
(c) Mach Number

(d) Angle of Attack and Sideslip - Coast and SIAD Flight

(e) Dynamic Pressure

(f) Angle of Attack and Sideslip - PDD Flight

Figure 11: Reconstructed Trajectory States

a thrust-like force was applied to the vehicle with a duration of approximately 1 s. The force occurs mainly in the axial direction, with a magnitude of roughly 10% of the STAR-48 full thrust or equivalently a 50% reduction in drag. Small lateral components were responsible for inducing the vehicle oscillations, which were initiated shortly after the thrust-like force was applied as shown in Figure 12(e). These oscillations continued throughout the coast phase of flight. After SIAD deployment, the vehicle static stability increased,

which had the effect of reducing the oscillation amplitude and increasing the frequency.

A similar event occurred approximately 4 s after PDD deployment. At a time of approximately 146 s, a sudden increase in sensor noise can clearly be seen in Figures 12(b) and 12(d). The character of the vehicle oscillation changes somewhat, possibly due to non-zero mean force acting on the vehicle. This disturbance leads to an increase in body rates, including a roll rate building up to approximately 20 deg/s. These force anomalies are possibly related, and the cause is currently under investigation.
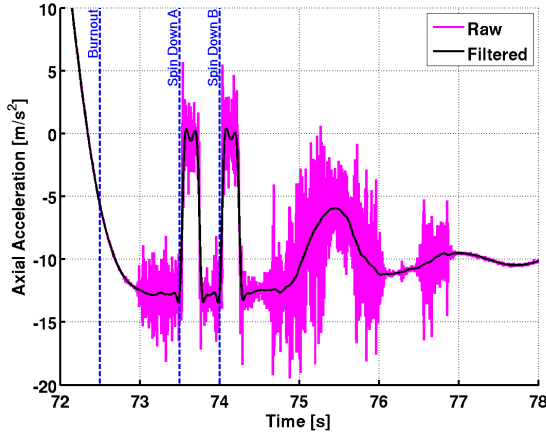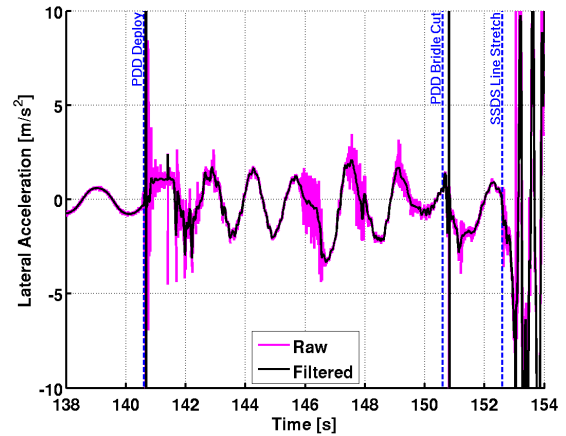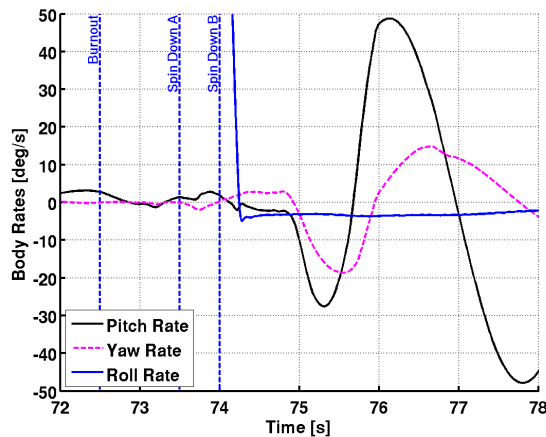

(a) Axial Acceleration: First Anomaly
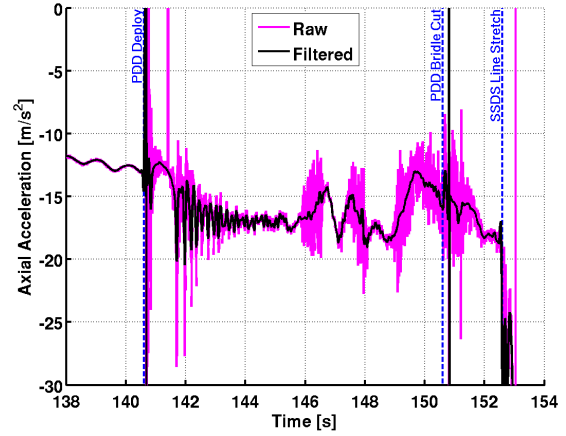
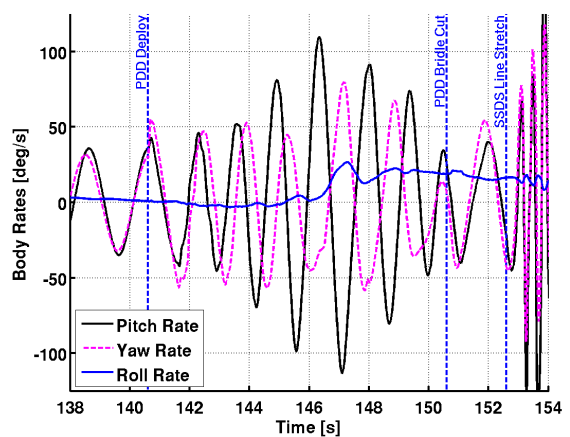(b) Axial Acceleration: Second Anomaly
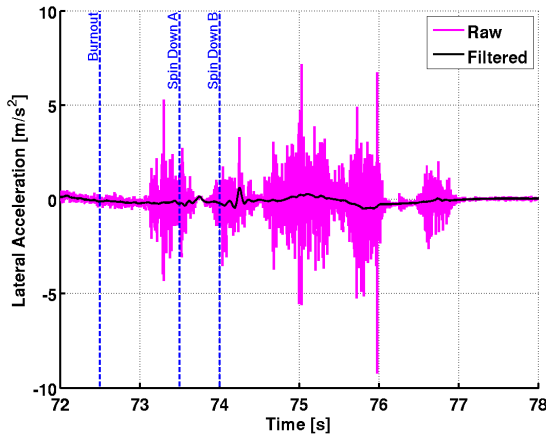
(c) Lateral Acceleration: First Anomaly

(d) Lateral Acceleration: Second Anomaly

(e) Body Rates: First Anomaly

(f) Body Rates: Second Anomaly

Figure 12: Accelerations and Rates During Force Anomalies

12

Reconstructed Thrust

The reconstructed thrust from the STAR-48 based on the chamber pressure measurement was found to be corrupted by the presence of transducer errors. These errors are in the form of zero offsets and scale factors that result in thrust levels between 2-5% higher than prediction, resulting in an overall motor impulse that is 4% higher than predictions. This high level of impulse is far outside the confidence level of ATK in their ability to predict the total impulse, which is based largely on the mass of propellant in the motor and tends to be very well known. However, the shape of the reconstructed thrust was generally consistent with the preflight prediction. In addition, the thrust reconstructed from nominal aerodynamics matches very closely with the predictions in the high Mach regimes toward the end of the motor burn, where confidence in the aerodynamic models are best. These observations indicate that the chamber pressure measurement was biased. A correction factor was used to scale the measurement in order to remove zero offsets and to match the preflight impulse prediction.

The pressure measurement correction factor is given by the equation

$$P_c = \eta \left[\bar{P}_c - c_1 - c_2 \left(\frac{t - t_{ig}}{t_{bo} - t_{ig}} \right) \right] \tag{11}$$

where c_1 is the offset between the atmospheric pressure and the sensor measurement at motor ignition, the quantity $c_1 + c_2$ is the pressure offset after burnout, and $\bar{P}_c$ is the raw chamber pressure measurement. The scale factor η is specified such that the reconstructed motor impulse matches the preflight prediction, η = 0.9677.

Transient data around the time of ignition were also edited out and replaced with a 0.5 s segment from the nominal profile. These transients arose because that pressure transducer was mounted in the igniter and not actually in the chamber.
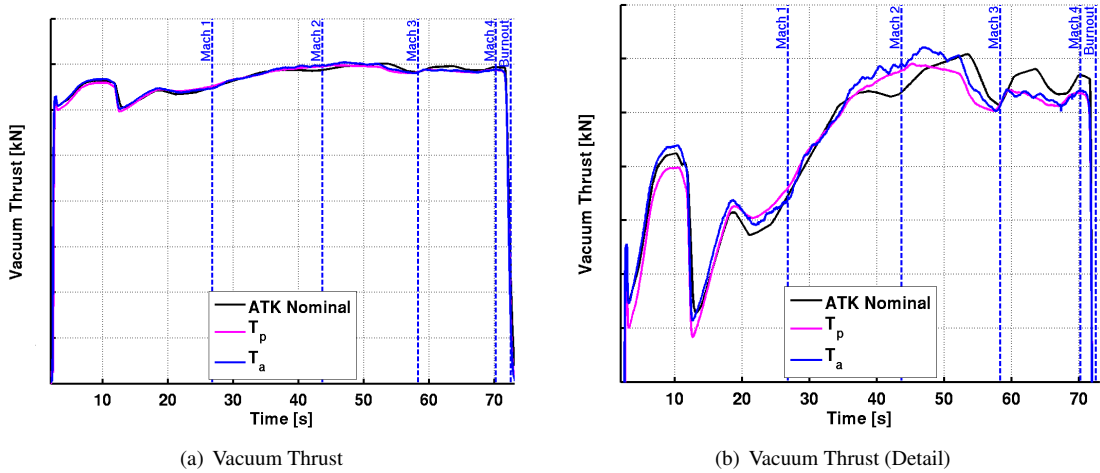

(a) Vacuum Thrust   (b) Vacuum Thrust (Detail)

Figure 13: Reconstructed Main Motor Thrust

The reconstructed thrust profiles are shown in Figure 13. The reconstructed thrust profiles are generally in good agreement with each other and with the preflight nominal profile, in terms of overall shape and total burn time. The total impulse derived from the thrust based on aerodynamics matches the preflight prediction to within 0.44%.

Reconstructed Aerodynamics

The vehicle aerodynamics were reconstructed using the measured accelerations and angular rates and vehicle mass properties. During powered flight, the reconstructed STAR-48 motor thrust profile was used to separate the aerodynamic forces from the total forces measured by the IMU. The reconstructed axial force, side force, and pitch moment coefficients during powered flight are shown in the left columns of Figure 14. There are large discrepancies between the reconstruction and predicted aerodynamics early in the powered flight phase, which can be attributed to small dynamic pressure with relatively large uncertainties, and small aerodynamic forces relative to the STAR-48 thrust. The match improves as the Mach number and dynamic pressure increase. The reconstructed axial force coefficient is in good agreement with the predictions in the supersonic regime.

13

Note that the side force is clearly biased, even though the vehicle is oscillating about roughly a zero mean sideslip angle. A similar offset also appears in the normal force coefficient (not shown). This offset may be due to a thrust misalignment or a center of mass offset. A thrust misalignment of 0.26 deg, corresponding to a 2.6σ dispersion, would be required to reconcile these differences. Biases in the moment coefficients are indicative of wobbling or off-axis rotation.

(a) Axial Force Coefficient: Powered Phase

(b) Axial Force Coefficient: Coast and SIAD Phase

(c) Side Force Coefficient: Powered Phase

(d) Side Force Coefficient: Coast and SIAD Phase

(e) Pitch Moment Coefficient: Powered Phase
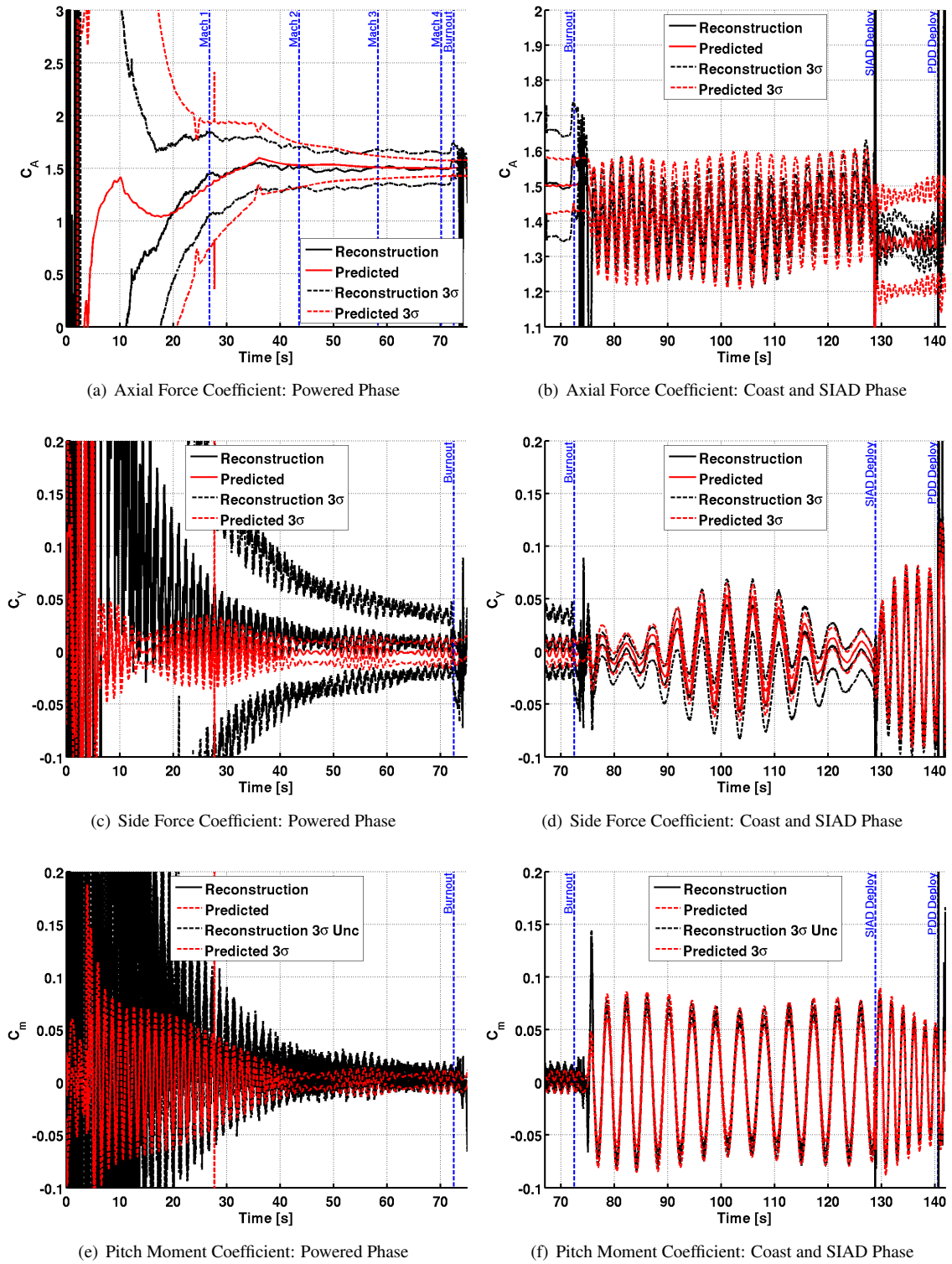
(f) Pitch Moment Coefficient: Coast and SIAD Phase

Figure 14: Reconstructed Aerodynamics

The reconstructed coast and SIAD phase aerodynamics are shown in the right column of Figure 14. The vehicle axial force coefficient and pitching moment coefficient are in fairly good agreement with the nominal aerodynamics during this phase. A bias in the side force coefficient can be seen. A similar bias is also evident in the yawing moment reconstruction, which could be indicative of a center of mass offset. During coast phase, the reconstructed force coefficients show a slightly lower peak to peak amplitude of oscillation. This trend reverses during SIAD flight phase, where the reconstruction force coefficients exhibit a slightly higher amplitude. The discrepancy in amplitude may be due to the sensitivity of aerodynamics to the TV aftbody geometry at large angles of attack. For simplicity, the coast and SIAD phase CFD grids did not model the annular base cavity of the flight article, and omission of this feature is likely to reduce the accuracy of computations as the angle of attack is increased from anticipated levels to those of SFDT-2.

Vehicle aerodynamic parameters during coast phase were estimated over a window of data from 78.5-128.5 s after drop. The equation error methodology described previously was employed to estimate a set of uncertainty factor inputs to the vehicle aerodynamic database that best match the reconstructed total force and moment coefficients. The uncertainty factors are normalized inputs to the aerodynamic database that consist of various adders and multipliers. The uncertainty factors are normalized such that a value of 0 corresponds to the nominal case, and ± 1 corresponds to a $\pm 3\sigma$ dispersion, respectively, based on a priori dispersion estimates. Similarly, vehicle aerodynamic parameters during SIAD flight were estimated over a window of data from 130-140 s after drop.

Table 3: Aerodynamic Parameter Estimates

Uncertainty Factor	Coast Phase	SIAD Phase
Axial Force Multiplier	-0.0996	0.0303
Normal Force Adder	-0.0959	-0.0589
Normal/Side Force Multiplier	-0.5722	0.6627
Side Force Adder	-0.7773	-0.5546
Pitch Moment Adder	-0.0226	0.1877
Pitch/Yaw Moment Multiplier	0.1911	0.1615
Yaw Moment Adder	-0.1412	-0.4573
Pitch/Yaw Damping Adder	-0.1517	-0.6959

(a) Side Force Coefficient During Coast Phase (b) Pitch Moment Coefficient During Siad Phase
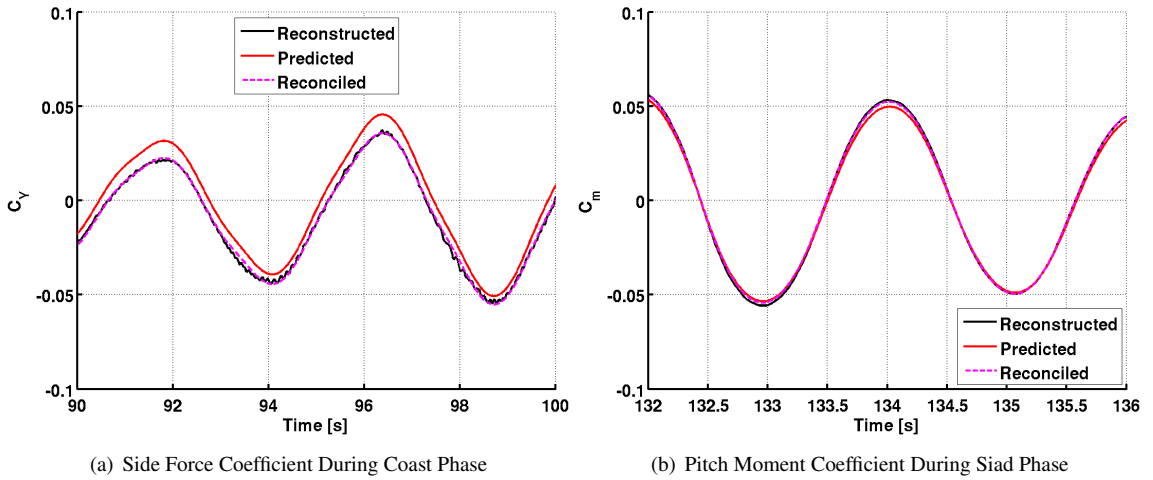
Figure 15: Reconciled Aerodynamics

The results of the parameter identification method are shown in Table 3, and example fits are shown in Figure 15. These results indicate that a reasonable set of dispersions can reconcile differences between the reconstructed and nominal aerodynamics. The largest of these dispersions is the coast phase side force adder of -2.33σ, although this value is confounded somewhat by the uncertainty in the vehicle center of mass. The

15

SIAD phase side force adder is consistent in sign but of a slightly lesser magnitude. The side/normal force multiplier is consistent with the amplitude differences that were noted in coast and SIAD flight, corresponding to -1.72σ and 1.99σ, respectively. The vehicle static stability (moment multiplier) is slightly higher than predicted in both coast and SIAD flight phases, at 0.57σ and 0.48σ, respectively. The damping adder indicates that the vehicle is more dynamically stable in both configurations as well, at -0.45σ and -2.08σ, respectively.

CONCLUSIONS

On June 8th, 2015, the Low Density Supersonic Decelerator project flew a second full-scale flight test known as the Supersonic Flight Dynamics Test. The sensor measurements acquired during the flight test were of good quality, allowing a vehicle trajectory, atmosphere, thrust, and aerodynamic reconstruction to be performed. The reconstructed trajectory was a critical input to the post-flight simulation model reconciliation effort. The results of the reconciliation led to several important modeling updates, which will be utilized for pre-flight targeting and launch operations for the third planned flight test.

ACKNOWLEDGEMENTS

NOTATION

A_e	STAR-48 nozzle exit area
A_t	STAR-48 nozzle throat area
a_x, a_y, a_z	body axis accelerations at the vehicle CG
C_A, C_Y, C_N	axial, side, and normal force coefficients
C_F	STAR-48 thrust coefficient
C_l, C_m, C_n	roll, pitch, and yaw moment coefficients
c_1, c_2	STAR-48 pressure measurement correction coefficients
d	reference diameter of test vehicle
$\boldsymbol{I}$	vehicle inertia
$\mathcal{M}$	Mach number
m	mass of test vehicle
P_c	STAR-48 chamber pressure
P_e	ambient pressure at the STAR-48 nozzle exit
p, q, r	body axis angular rates
S	reference area of test vehicle
T_a	STAR-48 vacuum thrust reconstructed from accelerations and nominal aerodynamics
T_p	STAR-48 vacuum thrust reconstructed from chamber pressure measurement
t	time from test vehicle drop
t_{bo}	time of STAR-48 burnout
t_{ig}	time of STAR-48 ignition
$\boldsymbol{u}$	aerodynamic uncertainty factor
α	angle of attack
β	angle of sideslip
η	STAR-48 pressure measurement multiplier

REFERENCES

[1] Clark, I. G., Adler, M., and Rivellini, T. P., "Development and Testing of a New Family of Supersonic Decelerators," AIAA Paper 2013-1252, March 2013.

[2] Kutty, P., Karlgaard, C. D., Blood, E., O'Farrell, C., Ginn, J., Schoenenberger, M., and Dutta, S., "Supersonic Flight Dynamics Test: Trajectory, Atmosphere, and Aerodynamics Reconstruction," American Astronautical Society, AAS Paper 15-224, January 2015.

[3] Blood, E., Ivanov, M., O'Farrell, C., Ginn, J., Kutty, P., Karlgaard, C., and Dutta, S., "LDSD Supersonic Flight Dynamics Test 1: Post-flight Reconstruction," IEEE Aerospace Conference, Paper 2621, March 2015.

[4] Ivanov, M. C., Blood, E. M., Cook, B. T., Giersch, L. R., Grover, M. R., Jakobowski, J. K., Rivellini, T. P., Su, R. P., Samareh, J. A., Zang, T. A., Winski, R. G., Olds, A. D., and Kinney, D. J., "Entry, Descent and Landing Systems Analysis Study: Phase 2 Report on Mars Science Laboratory Improvement," NASA TM-2011-216988, January 2011.

[5] White, J., Bowes, A., Dutta, S., Ivanov, M., Queen, E., Powell, R., and Striepe, S., "LDSD POST2 Modeling Enhancements in Support of SFDT-2 Flight Operations," American Astronautical Society, AAS Paper 16-221, February 2016.

[6] Clark, I. and Adler, M., Summary of the Second, High-Altitude Supersonic Flight Dynamics Test for the LDSD Project," IEEE Aerospace Conference, March 2016.

[7] Dutta, S., Bowes, A., White, J., Striepe, S., Queen, E., O'Farrell, C., and Ivanov, M., "Post-flight Assessment of Low Density Supersonic Decelerator Flight Dynamics Test 2 Simulation," American Astronautical Society, AAS Paper 16-222, February 2016.

[8] Van Norman, J. W., Dyakonov, A., Schoenenberger, M., Davis, J., Muppidi, S., Tang, C., Bose, D., Mobley, B., and Clark, I., "Aerodynamic Models for the Low Density Supersonic Decelerator (LDSD) Test Vehicles," American Institute of Aeronautics and Astronautics, AIAA Paper, June 2016.

[9] Anon., "NASA Sounding Rocket Program Handbook," Sounding Rockets Program Office, Suborbital and Special Orbital Projects Directorate, Goddard Space Flight Center, Wallops Flight Facility, Wallops Island, Virginia, 810-HB-SRP, June 2005.

[10] Hedin, A. E., "Extension of the MSIS Thermosphere Model into the Middle and Lower Atmosphere," *Journal of Geophysical Research*, Vol. 96, No. A2, 1991, pp. 1159-1172.

[11] Karlgaard, C. D., Tartabini, P. V., Blanchard, R. C., Kirsch, M., and Toniolo, M. D., "Hyper–X Post–Flight Trajectory Reconstruction," *Journal of Spacecraft and Rockets*, Vol. 43, No. 1, 2006, pp. 105–115.

[12] Karlgaard, C. D., Tartabini, P. V., Martin, J. G., Blanchard, R. C., Kirsch, M., Toniolo, M. D., and Thornblom, M. N., "Statistical Estimation Methods for Trajectory Reconstruction: Application to Hyper-X," NASA TM-2009-215792, August 2009.

[13] Karlgaard, C. D., Beck, R. E., Derry, S. D., Brandon, J. M., Starr, B. R., Tartabini, P. V., and Olds, A. D., "Ares I-X Trajectory Reconstruction: Methodology and Results," *Journal of Spacecraft and Rockets*, Vol. 50, No. 3, 2013, pp. 641–661.

[14] Karlgaard, C. D., Kutty, P., Schoenenberger, M., Munk, M. M., Little, A., Kuhl, C. A., and Shidner, J., "Mars Science Laboratory Entry Atmospheric Data System Trajectory and Atmosphere Reconstruction," *Journal of Spacecraft and Rockets*, Vol. 51, No. 4, 2014, pp. 1029–1047.

[15] Wagner, W. E., "Re-Entry Filtering, Prediction, and Smoothing," *Journal of Spacecraft and Rockets*, Vol. 3, No. 9, 1966, pp. 1321–1327.

[16] Wagner, W. E. and Serold, A. C., "Formulation on Statistical Trajectory Estimation Programs," NASA CR-1482, January 1970.

[17] Olds, A. D., Beck, R. E., Bose, D. M., White, J. P., Edquist, K. T., Hollis, B. R., Lindell, M. C., Cheatwood, F. M., Gsell, V. T., and Bowden, E. L., "IRVE-3 Post-Flight Reconstruction," AIAA Paper 2013-1390, March 2013.

[18] Heck, M. L., Findlay, J. T., Kelly, G. M., and Compton, H. R., "Adaptation of a Strapdown Formulation for Processing Inertial Platform Data," *Journal of Guidance, Control, and Dynamics*, Vol. 7, No. 1, 1984, pp. 15–19.

[19] Sutton, G. P., *Rocket Propulsion Elements*, John Wiley & Sons, New York, 1992.

[20] Klein, V. and Morelli, E. A., *Aircraft System Identification: Theory and Practice*, AIAA, August 2006.

[21] Leslie, F. W. and Justus, C. G., "The NASA Marshall Space Flight Center Earth Global Reference Atmospheric Model - 2010 Version," NASA TM-2011-216467, June 2011.